Chemical Science

ROYAL SOCIETY OF CHEMISTRY

EDGE ARTICLE

View Article Online
View Journal | View Issue

Cite this: *Chem. Sci.*, 2023, **14**, 903

All publication charges for this article have been paid for by the Royal Society of Chemistry

Catalyst-free synthesis of diverse fluorescent polyoxadiazoles for the facile formation and morphology visualization of microporous films and cell imaging†

Junyao Xie,[a] Niu Niu,[ab] Xinyao Fu,[c] Xiang Su,[a] Dong Wang,[a] Anjun Qin,[c] Ting Han*[a] and Ben Zhong Tang*[d]

The development of facile polymerizations toward functional heterocyclic polymers is of great significance for chemistry and materials science. As an important class of heterocyclic polymers, polyoxadiazoles (PODs) have found applications in various fields. However, the synthetic difficulties of PODs greatly restrict their structural diversity and property investigation. Herein, we report a series of catalyst-free multicomponent polymerizations (MCPs) that can facilely synthesize functional PODs with well-defined and diversified topological structures from commercially available or readily accessible aldehydes, carboxylic acids, secondary amines, and (*N*-isocyanimino)triphenylphosphorane at room temperature. Unlike conventional Ugi polycondensations, the present Ugi-type MCPs can *in situ* generate oxadiazole moieties in polymer backbones. The obtained PODs possess good solubility, high thermal and morphological stability, and excellent film-forming ability. The introduction of aggregation-induced emission (AIE) moieties together with the inherent structural features of PODs endow these polymers with multiple functionalities. The AIE-active linear PODs can form fluorescent microporous films with stable and ordered structures based on the simple breath figure patterning method, and the self-assembly morphologies can be directly visualized by fluorescence microscopy in a high-contrast and sensitive manner. Moreover, both the linear and hyperbranched AIE-active PODs possess excellent biocompatibility, good lysosome specificity, and excellent photobleaching resistance, which enable them to serve as promising lysosome-specific fluorescent probes in biological imaging.

Received 27th October 2022
Accepted 19th December 2022

DOI: 10.1039/d2sc05960f

rsc.li/chemical-science

Introduction

The development of facile polymerization methods for the construction of functional synthetic polymers with unique structures and attractive properties is of great academic and industrial significance. Among various functional polymers, heterocyclic polymers have gained tremendous attention for decades due to their wide applications in diverse fields.[1–5] The presence of heterocycles or fused heterocycles in polymer backbones could endow such polymers with excellent thermal and mechanical performance, unique electronic and photophysical properties, high chemical stability, and stimuli-responsive characteristics. To date, a large variety of functional heterocyclic polymers have been developed, such as polyimides, polybenzothiadiazoles, polypyrroles, polyquinolines, polythiophenes, and polybenzimidazoles. As an important class of heterocyclic polymers, polyoxadiazoles (PODs) with conjugated heterocyclic rings have been widely studied in heat-resistant materials, gas separation, fuel cells, acid sensors, polymer electroluminescent devices, electron and proton conducting materials, *etc.*, owing to their excellent film-forming ability and high chemical and thermal stability, as well as the specific properties determined by the oxadiazole ring.[6–11] By contrast, the photoluminescence (PL)-related applications such as fluorescence-based visualization and biological imaging have been significantly less explored for oxadiazole-based polymers, which might be due to the poor fluorescence of conjugated PODs in the aggregated state arising from their rigid polymer backbones and strong intermolecular π–π interactions.[12]

[a]*Center for AIE Research, Shenzhen Key Laboratory of Polymer Science and Technology, Guangdong Research Center for Interfacial Engineering of Functional Materials, College of Materials Science and Engineering, Shenzhen University, Shenzhen, 518060, China. E-mail: hanting@szu.edu.cn*

[b]*College of Physics and Optoelectronic Engineering, Shenzhen University, Shenzhen, 518060, China*

[c]*State Key Laboratory of Luminescent Materials and Devices, Guangdong Provincial Key Laboratory of Luminescence from Molecular Aggregates, Center for Aggregation-Induced Emission, AIE Institute, South China University of Technology, Guangzhou, 510640, China*

[d]*School of Science and Engineering, Shenzhen Institute of Aggregate Science and Technology, The Chinese University of Hong Kong, Shenzhen, Guangdong, 518172, China. E-mail: tangbenz@cuhk.edu.cn*

† Electronic supplementary information (ESI) available. See DOI: https://doi.org/10.1039/d2sc05960f

Most application scenarios in real life require the PL materials to be used as solid films or in aqueous media. Therefore, the development of functional PODs with efficient aggregate-state fluorescence and the exploration of their PL-related advanced applications are highly desirable.

The creation of polymer materials with new structures and desired properties often relies on expedient synthetic strategies. Traditional synthetic methods toward PODs typically include two types. One is the two-step method, in which a polyhydrazide was first prepared through the polymerization of a dicarboxylic acid chloride with a dihydrazide at low temperature in a polar solvent such as *N*-methylpyrrolidone (NMP), and then the polyhydrazide underwent the cyclodehydration reaction at high temperature using dehydrating agents to afford PODs (Fig. 1A, method I).[10,13] This method can effectively control the structures of POD products, but the synthetic procedures are tedious and the starting materials are limited and relatively high-cost. The other method can directly afford POD derivatives through the polycyclocondensation reactions of dicarboxylic acids and hydrazine sulphate in the presence of poly(phosphoric acid) (PPA) or oleum (Fig. 1A, method II).[6,14] However, this one-step method still needs to be conducted under heating conditions and hydrazine sulphate is toxic and difficult to handle. Moreover, these two methods are not very conducive to the flexible design and adjustment of POD structures, and the POD structure and the polyhydrazide block could simultaneously exist in the polymeric products. These synthetic difficulties greatly restrict the structural diversity and property investigation of PODs.

In recent years, multicomponent polymerizations (MCPs) have emerged as powerful tools for the synthesis of structurally well-defined and complex polymers with the merits of simple operation, mild reaction conditions, good functional-group tolerance, and high efficiency. The structural diversity and functionalities of MCP products can be readily tuned by changing the structures or combinations of multiple monomers.[15] Benefiting from the advantages of MCPs, various multifunctional polymers that are difficult or troublesome to obtain by traditional methods were constructed.[16–23] As one of the well-known MCPs, Ugi polymerization of acids, amines, isocyanides, and aldehydes or ketones has attracted tremendous attention since its first report in 2014 (Fig. 1B).[24–26] By rationally designing the monomer structures or combinations, a series of Ugi-type MCPs have been developed for the preparation of polyamides and polypeptoids.[27–33] However, the product structures of Ugi-type polycondensations are generally limited to diverse polyamide derivatives with linear structures. Examples of the synthesis of functional heterocyclic polymers with different topological structures by Ugi-type polycondensations are still very rare.

MCPs are generally developed from appropriate multicomponent reactions (MCRs). Recently, a facile and efficient Ugi-type MCR method for the synthesis of oxadiazole derivatives has caught our attention. As shown in Scheme S1,† the catalyst-free MCR of an aromatic aldehyde, carboxylic acid, secondary amine, and (*N*-isocyanimino)triphenylphosphorane can afford 2,5-disubstituted 1,3,4-oxadiazoles at room temperature by a sequence of the Ugi four-component reaction and an intramolecular aza-Wittig ring closure.[34] The introduction of such a unique heterocyclic skeleton into polymer main chains is envisioned to endow the corresponding polymer materials with a variety of interesting properties and advanced functionalities.

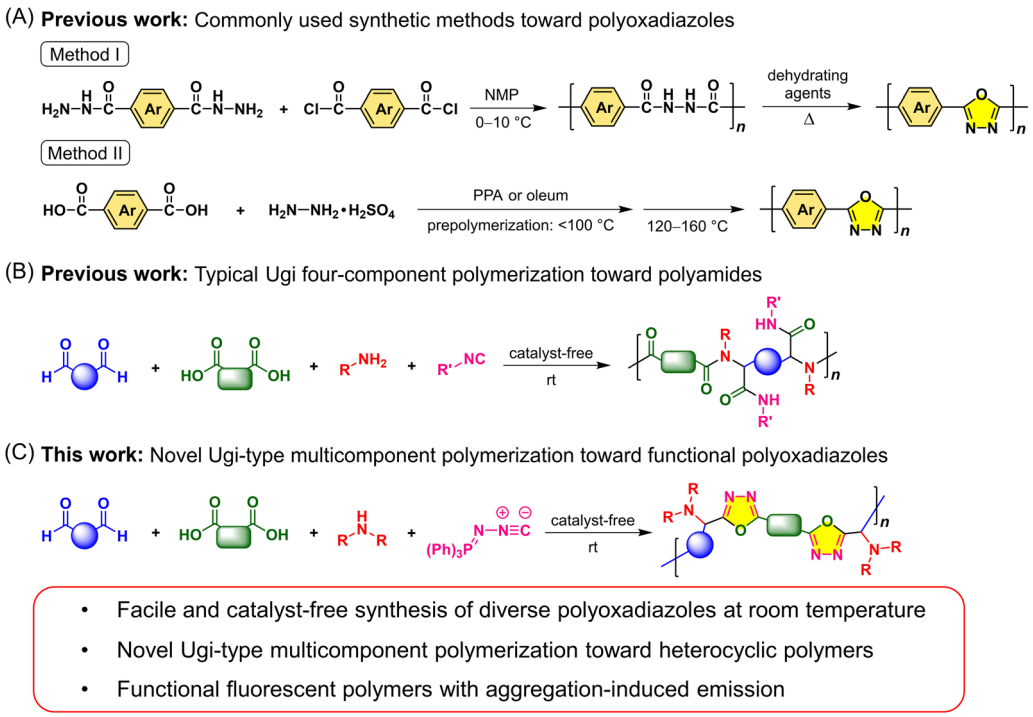

Fig. 1 Comparison between (A and B) the previous work on the synthesis of polyoxadiazole and the typical Ugi polymerization and (C) the novel Ugi-type polymerization toward fluorescent polyoxadiazoles developed in this work.

For instance, the non-conjugated backbone structures with distorted conformations and multiple large substituents might inherently block the formation of strong interchain π–π interactions, which would be conducive to the improvement of solubility and aggregate-state fluorescence of oxadiazole-based polymers. Moreover, the readily available starting materials, mild reaction conditions, and simple operation would make the corresponding polymerization method a feasible tool for the flexible design and functionalization of diverse POD structures, thereby providing new possibilities for the study on the structure–property relationship and applications of functional heterocyclic polymer materials.

With these concerns in mind, herein we successfully develop this MCR into a novel Ugi-type MCP tool to benefit the synthesis of diverse functional POD derivatives (Fig. 1C). Taking advantage of the wide monomer scope and various monomer combinations of the MCP method, a series of fully substituted PODs with well-defined and diversified topological structures are facilely synthesized from commercially available or readily accessible aldehydes, carboxylic acids, secondary amines, and (*N*-isocyanimino)triphenylphosphorane at room temperature without using any catalyst. Different from the typical Ugi polycondensations, the use of (*N*-isocyanimino)triphenylphosphorane as the isocyanide input and a secondary amine as the amine input is critical for the present Ugi-type MCP strategy, which allows the imino-anhydride intermediate to undergo an intramolecular aza-Wittig reaction rather than the Mumm rearrangement.[35] The obtained PODs possess good solubility, high thermal and morphological stability, and excellent film-forming ability. By appropriately introducing fluorescent moieties with aggregation-induced emission (AIE) characteristics into the polymer structures, the resulting PODs showed efficient aggregate-state fluorescence and can be used in different PL-related advanced applications. The obtained AIE-active linear POD was demonstrated to possess interesting self-assembly properties and its thin films can readily form fluorescent patterns with stable and ordered porous structures on rainy days or based on the simple breath figure (BF) patterning method. These self-assembly morphologies can be directly visualized by fluorescence microscopy in a sensitive, on-site and real-time manner. To the best of our knowledge, this is the first report of the application of PODs for the fabrication of fluorescent microporous thin films using the BF method. Besides, the application potential of the fluorescent nanoparticles (NPs) of PODs in biological imaging was explored, demonstrating that both the linear and hyperbranched AIE-active PODs can serve as promising lysosome-specific fluorescent probes.

Results and discussion

Polymerization

To develop the Ugi-type polymerization route for the facile and efficient synthesis of PODs, we first optimized the polymerization conditions using the commercially available and inexpensive terephthalaldehyde (**1a**), terephthalic acid (**2a**), dibenzylamine

Table 1 Optimization of the multicomponent polymerization of **1a**, **2a**, **3a**, and **4**[a]

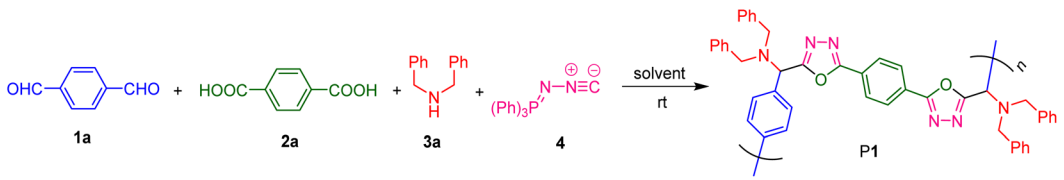

Entry	Solvent	[**1a**][b] (M)	[**1a**]/[**2a**]/[**3a**]/[**4**]	Atmosphere	Yield (%)	M_n[c] (MALLS)	M_w[c] (MALLS)	$Đ$[c]
1[d]	DCM	0.10	1.0/1.0/2.4/2.4	N_2	62	29 300	45 900	1.6
2	DMSO	0.10	1.0/1.0/2.4/2.4	N_2	74	24 800	37 100	1.5
3[d]	DMF	0.10	1.0/1.0/2.4/2.4	N_2	55	29 400	57 100	1.9
4[d]	DMAc	0.10	1.0/1.0/2.4/2.4	N_2	52	12 500	20 800	1.7
5[d]	THF	0.10	1.0/1.0/2.4/2.4	N_2	57	77 400	140 000	1.8
6[d]	THF/MeOH	0.10	1.0/1.0/2.4/2.4	N_2	32	27 100	40 700	1.5
7	DMSO	0.18	1.0/1.0/2.4/2.4	N_2	58	14 900	24 200	1.6
8	DMSO	0.22	1.0/1.0/2.4/2.4	N_2	59	12 800	20 000	1.6
9	DMSO	0.34	1.0/1.0/2.4/2.4	N_2	66	9100	13 400	1.5
10	DMSO	0.47	1.0/1.0/2.4/2.4	N_2	68	8500	11 700	1.4
11	DMSO	0.10	1.0/1.0/2.0/2.0	N_2	64	9900	14 000	1.4
12	DMSO	0.10	1.0/1.0/3.0/3.0	N_2	50	7900	11 800	1.5
13	DMSO	0.10	1.0/1.0/2.4/2.4	Air	55	31 300	72 200	2.3
14[e]	DMSO	0.10	1.0/1.0/2.4/2.4	N_2	76	25 000	50 100	2.0
15[f]	DMSO	0.10	1.0/1.0/2.4/2.4	N_2	69	19 200	34 800	1.8

[a] Unless otherwise noted, the polymerizations were carried out at room temperature for 24 h. [b] Monomer concentration was calculated considering the volume of both the solvent and the amine liquid. [c] Absolute molecular weights were determined by GPC using a multi-angle laser light scattering (MALLS) detector in THF. Dispersity ($Đ$) = M_w/M_n. [d] Unidentified structures exist in the polymeric products. [e] The reaction proceeded for 36 h. [f] The reaction proceeded for 48 h. Abbreviation: DCM = dichloromethane; DMSO = dimethyl sulfoxide; DMAc = *N*,*N*-dimethylacetamide; THF = tetrahydrofuran.

(**3a**), and (*N*-isocyanimino)triphenylphosphorane (**4**) as the model monomer combination. The polymerizations were all carried out at room temperature in a one-pot manner without using any catalyst or additive. As summarized in Table 1, the effects of various polymerization parameters on the polymerization efficiency were systematically investigated, including solvent, reactant concentration, monomer feed ratio, reaction atmosphere, and time course.

In the first attempt, the polymerization of **1a**, **2a**, **3a**, and **4** was carried out in dichloromethane (DCM) under N_2 at a monomer concentration of [**1a**] = 0.1 M and the monomer molar ratio of [**1a**] : [**2a**] : [**3a**] : [**4**] was 1.0 : 1.0 : 2.4 : 2.4. Under such conditions, a high molecular weight polymer with an absolute number-average molecular weight (M_n) of 293 000 and an absolute weight-average molecular weight (M_w) of 45 900 was produced in 62% yield after 24 h (Table 1, entry 1). However, there exist some unidentified structures in the product obtained from the polymerization in DCM. We then tried to carry out the polymerization reaction in DMSO, DMF, DMAC, THF, and the THF/MeOH mixture with a volume ratio of 1 : 1 (Table 1, entries 2–6). All these solvents can afford polymeric products, but only DMSO solvent can produce the purest polymeric product with the desired structure of the POD derivative (**P1**). Therefore, DMSO was chosen as the optimal solvent for the following investigation. Next, the effect of monomer concentration on polymerization was examined. As listed in entries 7–10 of Table 1, when the concentration of **1a** was gradually increased from 0.10 M to 0.47 M without changing the monomer feed ratio, both the reaction yield and the molecular weights of the product were decreased. Thus, the influence of the monomer feed ratio was then studied at a monomer concentration of [**1a**] = 0.10 M. The results shown in entries 2, 11 and 12 of Table 1 suggested that neither decreasing nor increasing the monomer ratio can give better polymerization results. We thus chose [**1a**] : [**2a**] : [**3a**] : [**4**] = 1.0 : 1.0 : 2.4 : 2.4 as the optimal monomer feed ratio. Considering that no air-sensitive monomer or catalyst was involved in this room temperature MCP, the polymerization was next carried out in air to further simplify the experimental procedure. The polymerization result indicated that this MCP is tolerant to air (entry 13, Table 1). Compared with the product obtained under nitrogen (entry 2, Table 1), the polymerization yield was decreased although the molecular weights were obviously increased under air. Finally, the time course of the polymerization was investigated under N_2 with the aim of further improving the reaction yield (Table 1, entries 2, 14 and 15). The results suggested that no significant improvement was achieved by prolonging the reaction time. Therefore, 24 h was adopted as the preferred reaction time for the MCP of **1a**, **2a**, **3a**, and **4**.

To explore the monomer scope of this catalyst-free MCP and meanwhile to enrich the structural diversity and functionalities of polymeric products, we then performed the polymerizations using various readily accessible dialdehydes, aromatic

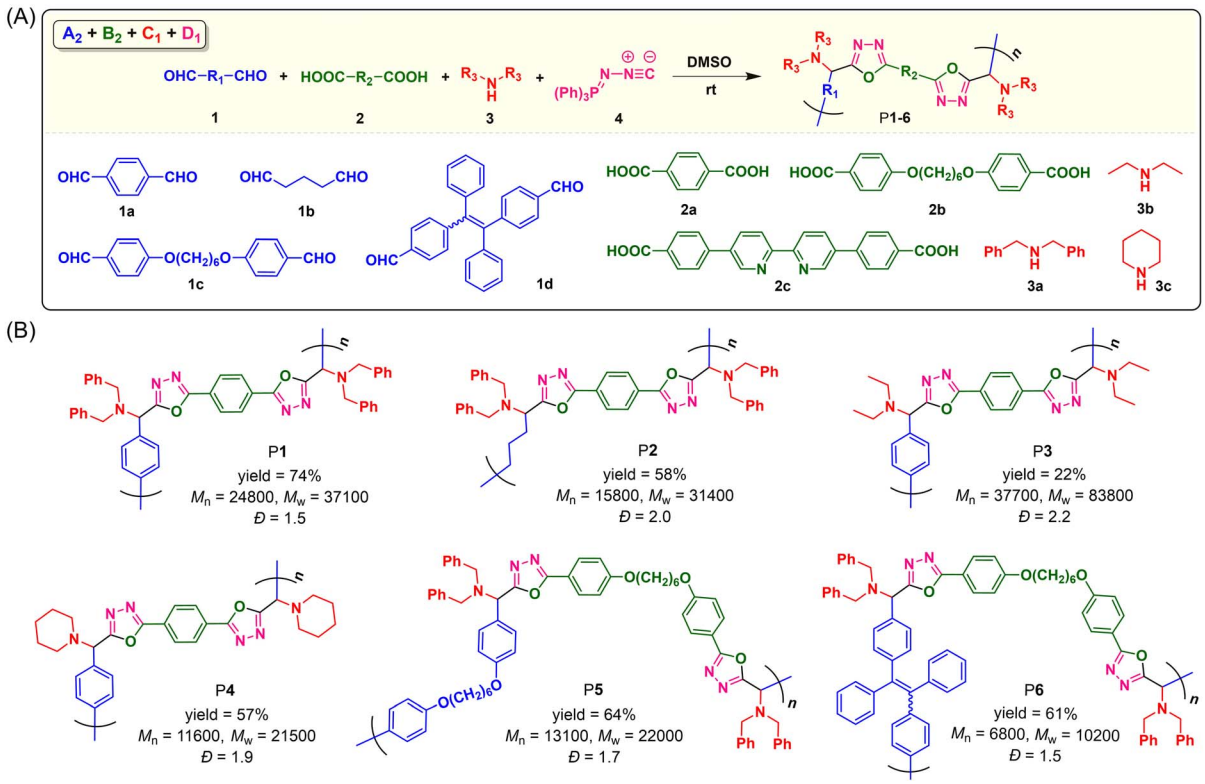

Fig. 2 (A) Catalyst-free multicomponent polymerizations of dialdehydes, dicarboxylic acids, secondary amines, and (*N*-isocyanimino)triphenylphosphorane. (B) Chemical structures, yields, molecular weights, and the dispersity of polymers **P1–6**. The polymerizations were carried out in DMSO at room temperature under N_2 for 24 h, [**1**] = 0.10 M, [**1**]/[**2**]/[**3**]/[**4**] = 1/1/2.4/2.4. Absolute molecular weights were determined by GPC using a multi-angle laser light scattering (MALLS) detector in THF. Dispersity ($Đ$) = M_w/M_n.

dicarboxylic acids, and secondary aliphatic diamines as monomers (Fig. 2A). The polymerization results shown in Fig. 2B suggested that this MCP can be applied to a wide variety of monomers. Under the optimized conditions, the MCPs of **1a–d**, **2a and b**, **3a–c**, and **4** generally proceeded smoothly at room temperature under N_2, producing a series of linear PODs **P1–P6** with high absolute M_ws of up to 83 800 in moderate yields of up to 74%. Both aromatic and aliphatic dialdehydes were suitable for this polymerization method, and the MCP of tetraphenylethylene (TPE)-containing aromatic dialdehyde (**1d**), aromatic dicarboxylic acid with alkoxy chain (**2b**), dibenzylamine (**3a**), and **4** can afford the TPE-functionalized linear POD with a M_w of 10 200 and a narrow dispersity of 1.5. However, when 4,4′-([2,2′-bipyridine]-5,5′-diyl)dibenzoic acid (**2c**) was adopted to react with monomers **1d**, **3a** and **4**, a polymeric product with poor solubility and an impure structure was obtained, possibly due to the poor solubility and reactivity of **2c** for this MCP. The other obtained polymers (**P1–P6**) all possess good solubility. They can be well dissolved in commonly used organic solvents such as THF, DMSO, DCM, $CHCl_3$, and DMF.

In addition to the synthesis of linear PODs based on the monomer combination of $A_2 + B_2 + C_1 + D_1$, we further explored the applicability of this MCP strategy using trifunctional and tetrafunctional monomers for the construction of hyperbranched polymers. As shown in Fig. 3, triphenylamine (TPA)-containing tricarboxylic acid (**2d**) and TPE-containing tetracarboxylic acid (**2e**) were synthesized to react with dialdehyde **1a** or **1d**, dibenzylamine **3a**, and **4**. Based on the above-mentioned optimized conditions, we first tried the monomer combination strategy of $A_2 + B_3 + C_1 + D_1$ by polymerizing **1a** (A_2), **2d** (B_3), **3a** (C_1), and **4** (D_1) in DMSO at room temperature under N_2 at a monomer concentration of [**1a**] = 0.10 M for 24 h. According to the Flory statistics,[36,37] the mole ratio of monomers could determine the gel point of such an "$A_2 + B_3$"-type polymerization system, and theoretically the problem of gelation could be overcome by using an equal molar ratio of A_2 and B_3.[38] Therefore, the polymerization was carried out with the monomer ratio of [**1a**] : [**2d**] : [**3a**] : [**4**] = 1.0 : 1.0 : 2.4 : 2.4. However, a partially soluble polymer was obtained in a yield of 50% (Table S1,† entry 1). A similar phenomenon was also observed when the TPE-containing dialdehyde **1d** was used to replace **1a** (Table S1,† entry 2). By changing the reaction condition to [**1a**] : [**2d**] : [**3a**] : [**4**] = 1.0 : 1.0 : 2.0 : 2.0 in a higher monomer concentration under air, high molecular weight hb-**P1** (M_n = 66 400 and M_w = 124 100) with good solubility was obtained in 66% yield after reacting for 24 h (Fig. 3A). Decreasing the reaction time from 24 h to 3 h led to a significant drop in molecular weights (Table S1,† entries 3 and 4). Under similar conditions, the polymerization of **1d**, **2d**, **3a** and **4** produced soluble hb-**P2** with a M_w of 8100 in 73% yield after 3 h (Table S1,† entry 5). Encouraged by

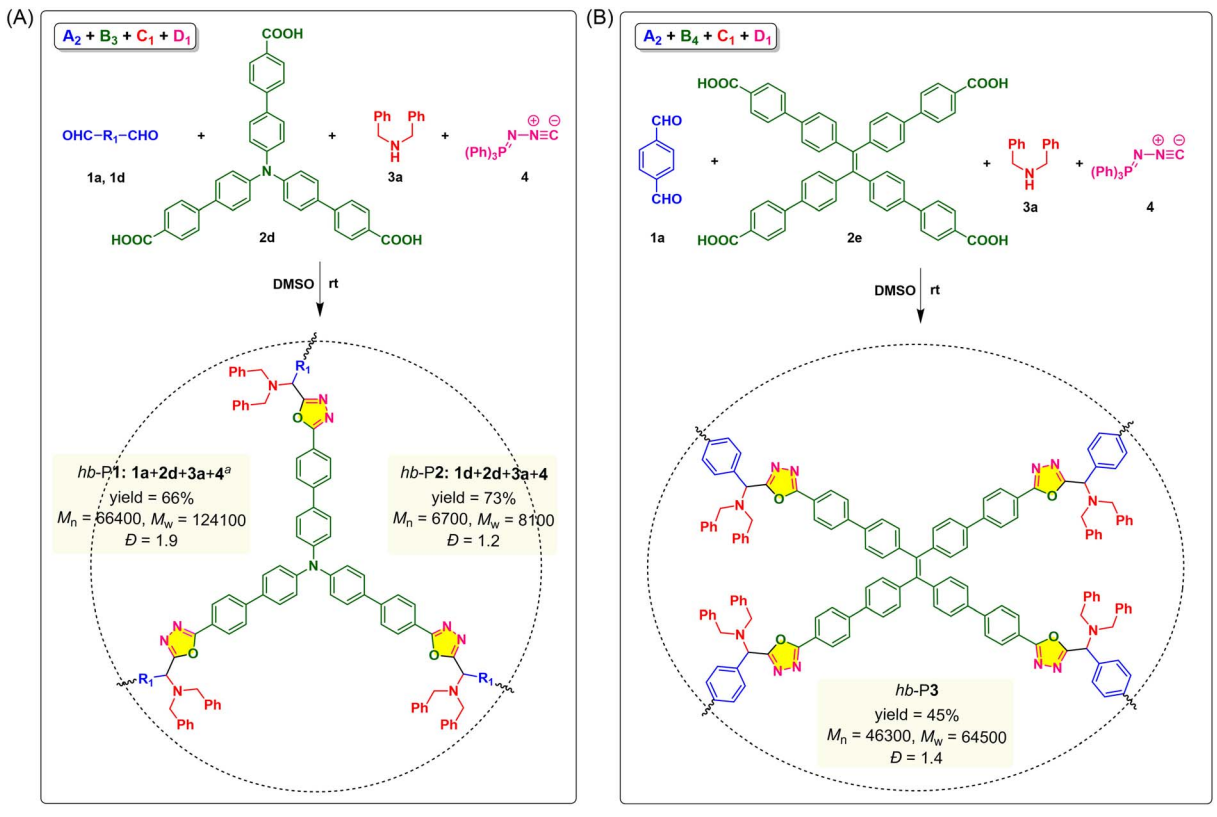

Fig. 3 Catalyst-free multicomponent polymerizations of aldehydes, carboxylic acids, secondary amines, and (*N*-isocyanimino)triphenylphosphorane through (A) $A_2 + B_3 + C_1 + D_1$ and (B) $A_2 + B_4 + C_1 + D_1$ manners. The polymerizations were carried out in DMSO at room temperature in air for 3 h, [**1**] = 0.18 M, [**1**]/[**2**]/[**3**]/[**4**] = 1.0/1.0/2.0/2.0. Absolute molecular weights were determined by GPC using a multi-angle laser light scattering (MALLS) detector in THF. Dispersity ($Đ$) = M_w/M_n. [a]Reaction time = 24 h.

these results, we then investigated the feasibility of the $A_2 + B_4 + C_1 + D_1$ monomer strategy to synthesize another TPE-containing hyperbranched POD (hb-**P3**) (Fig. 3B). As depicted in entries 6 and 7 of Table S1,† partially soluble polymeric products were obtained from the polymerization of **1a**, tetracarboxylic acid **2e**, **3a**, and **4** under the optimal conditions for linear polymers, while a soluble polymer with a high M_w of 64 500 was generated under air after reacting for 3 h. The successful synthesis of hb-**P1**–hb-**P3** demonstrated the general applicability of this catalyst-free MCP for the facile synthesis of hyperbranched polymers with diversified chemical and topological structures.

Structural characterization and thermal properties

To assist the structural characterization of the obtained polymers, model compound **5** was synthesized according to the synthetic route shown in Scheme S2.† The structures of model compound **5** and polymers were fully characterized and confirmed by IR, ^{1}H NMR, and ^{13}C NMR analysis. By comparing the characterization results of the polymers with those of **5** and the monomers, the polymeric products were demonstrated to possess the expected oxadiazole-containing structures. Detailed characterization data can be found in the ESI.† The IR, ^{1}H NMR and ^{13}C NMR spectra of **P1**, model compound **5**, and the corresponding monomers (**1a**, **2a**, **3a**, **4**) were compared and discussed here as an example. As shown in Fig. S1,† the peaks associated with the C=O stretching vibrations of **1a** and **2a** at 1685 and 1670 cm^{-1} and the broad absorption band corresponding to the O–H stretching vibration of COOH in **2a** all disappeared in the IR spectra of **P1**. Meanwhile, the characteristic peaks of the N–H and C≡N stretching vibrations of **3a** and **4** at 3320 and 2070 cm^{-1}, respectively, were also not detected after the polymerization. The IR spectrum of **P1** resembled that of model compound **5** to a large extent. These results clearly demonstrated the occurrence of this multicomponent polymerization.

More structural details could be revealed by the NMR spectra. As depicted in Fig. 4A–F, the ^{1}H NMR spectrum of **P1** showed no resonance of the –CHO proton of **1a** at δ 10.15. The resonance peaks associated with the –COOH proton of **2a** at δ 13.28 and the –NH– proton of **3a** at δ 2.59 also completely disappeared after the polymerization. Instead, a new peak emerged at δ 5.33 and δ 5.36 in the spectra of **5** and **P1**, respectively, which suggested the presence of newly formed methine groups (protons e and e′) in their structures. Regarding the ^{13}C NMR results (Fig. 4G–L), no resonance signal related to the C=O groups of **1a** and **2a** at δ 193.07 or 166.73 was observed in the ^{13}C NMR spectrum of **P1**. Moreover, the carbon resonance of the isocyanide group in **4** at

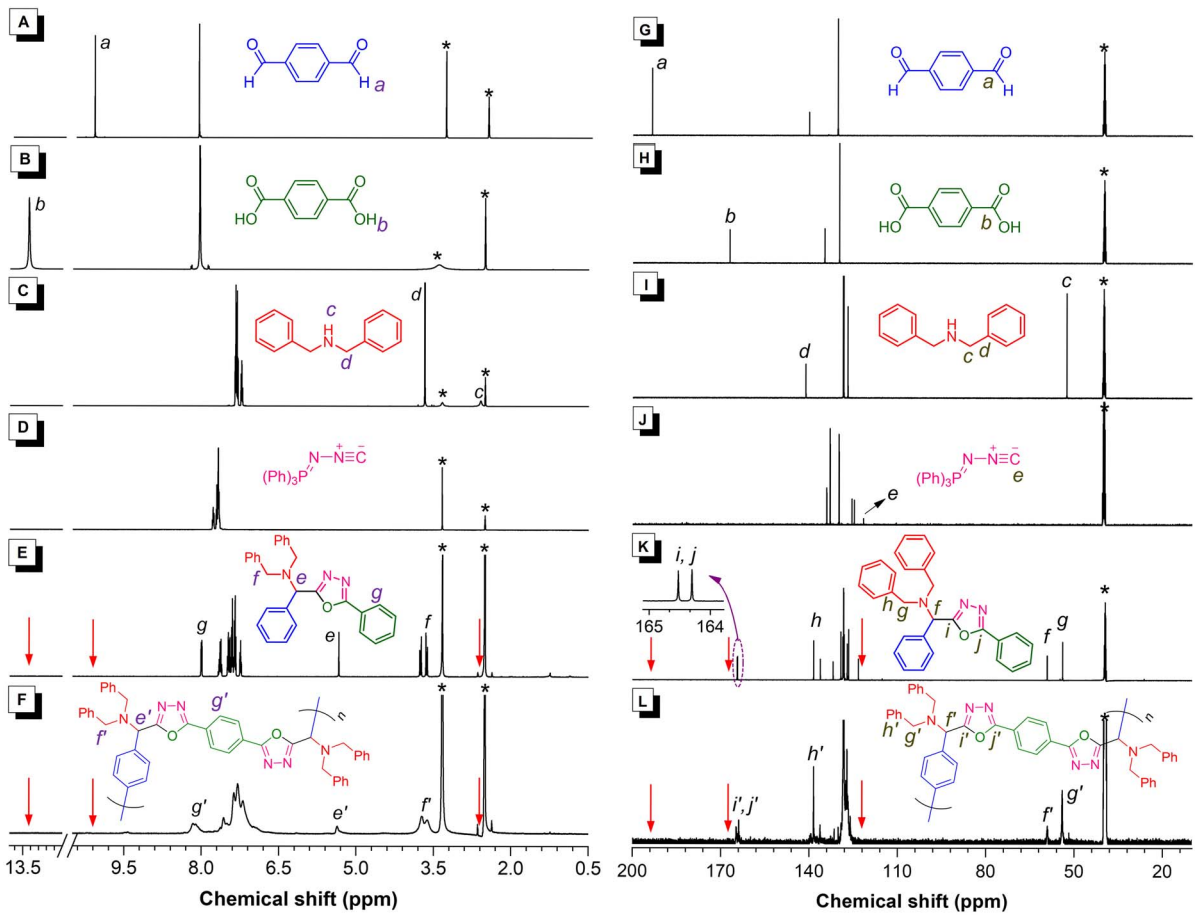

Fig. 4 (A–F) ^{1}H NMR spectra of (A) **1a**, (B) **2a**, (C) **3a**, (D) **4**, (E) model compound **5**, and (F) **P1** in DMSO-d_6. (G–L) ^{13}C NMR spectra of (G) **1a**, (H) **2a**, (I) **3a**, (J) **4**, (K) model compound **5**, and (L) **P1** in DMSO-d_6. The solvent peaks are marked with asterisks.

δ 121.16 disappeared and two adjacent peaks emerged at δ 164.77 and 163.89 for **P1** after the polymerization, which was in good accordance with the similar resonance peaks for **5** at δ 164.52 and 164.30 (carbons i and j). These results indicated the complete conversion from C═O and isocyanide to C═N bonds in the newly formed oxadiazole rings. Besides, a new peak associated with the methane carbon atom (positions f and f′) was observed at 59.18 and 59.10, respectively, in the ^{13}C NMR spectra of **5** and **P1**. Similarly, the IR, ^{1}H NMR and ^{13}C NMR results (Fig. S2–S7†) of the other polymers, including both the linear polymers (**P2–P6**) and the hyperbranched polymers (hb-**P1**–hb-**P3**) also showed the above-mentioned features. All these results confirmed the successful synthesis of PODs with the expected structures as depicted in Fig. 2 and 3.

The thermal stability of the resulting polymers was characterized by thermogravimetric analysis (TGA) under a nitrogen atmosphere at a heating rate of 10 °C min^{-1}. The TGA results depicted in Fig. S8† suggested that all these polymers possess good thermal stability. The decomposition temperature (T_d) at 5% weight loss of **P1–P6** and hb-**P1**–hb-**P3** located in the range of 237−300 °C and 257−272 °C, respectively, and their char yields reached up to 60 wt% at 600 °C. The glass transition temperatures (T_g) of these polymers were then measured using the differential scanning calorimetry (DSC) analysis. As summarized in Fig. S9,† the linear polymers **P1–P6** showed a similar T_g ranging from 96 to 98 °C, whereas the hyperbranched polymers hb-**P1–P3** showed much higher T_g values varying from 163 to 199 °C, possibly due to the presence of more complex intra- and inter-chain interactions among the hyperbranched polymer chains.

Photophysical properties

The absorption spectra of the obtained PODs in Fig. S10† suggested that **P1–P6** absorbed little light in the visible spectral region due to the weak electronic conjugation in their polymer backbones, and their maximum absorption wavelengths ($\lambda_{abs,max}$) were ranging from 281 to 330 nm. The $\lambda_{abs,max}$ of hyperbranched polymers (hb-**P1**–hb-**P3**) varied from 317 nm to 372 nm, among which hb-**P1** and hb-**P2** showed much longer absorption wavelengths due to the existence of a typical electron-donating moiety (TPA) in their structures.

In the past two decades, luminogens with AIE characteristics have received tremendous attention as functional fluorescent materials due to their advantages of efficient aggregate-state fluorescence and excellent photostability.[39,40] As an archetypical AIE luminogen, TPE is non-emissive in dilute solution but becomes highly fluorescent upon aggregation.[41] TPA is also a well-

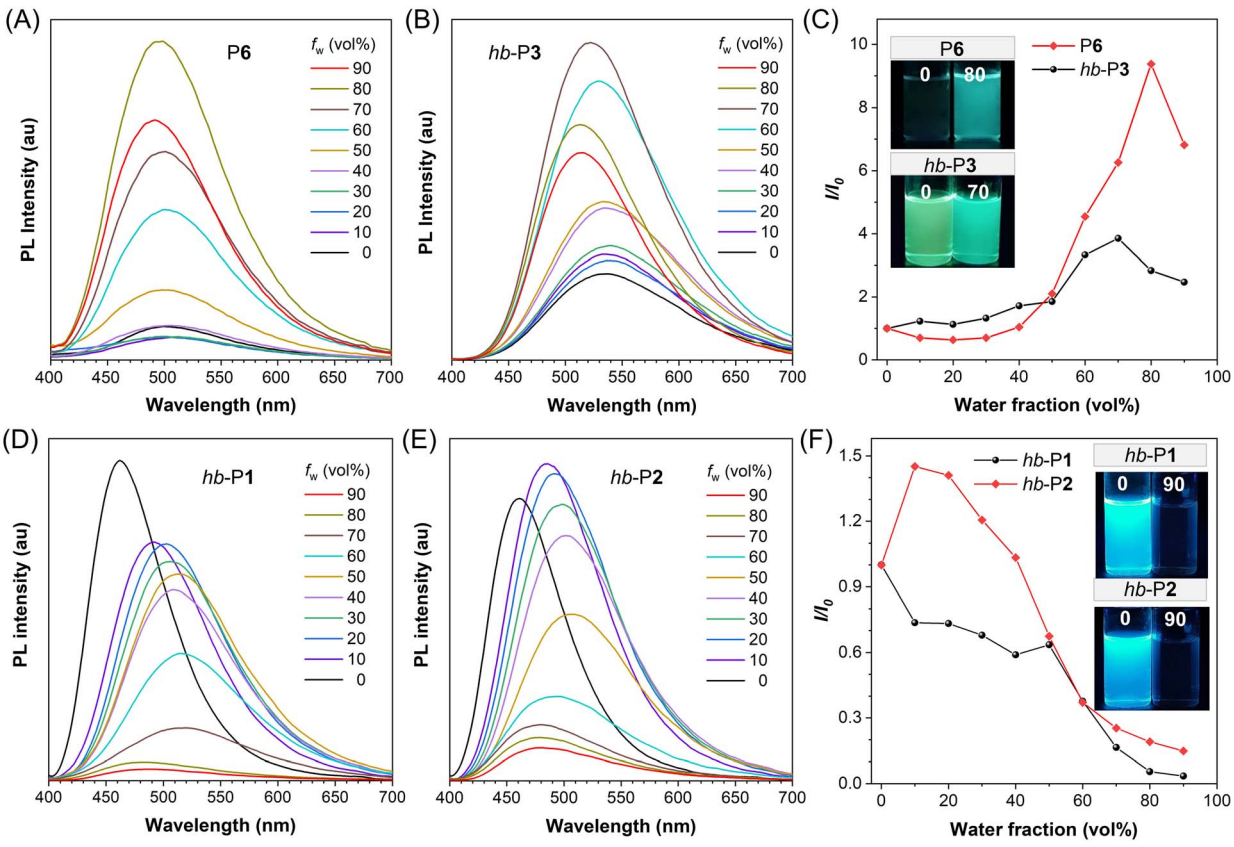

Fig. 5 (A, B, D and E) Photoluminescence (PL) spectra of (A) **P6**, (B) hb-**P3**, (C) hb-**P1**, and (D) hb-**P2** in THF/water mixtures with different water fractions (f_w). Solution concentration: 10 μM. Excitation wavelength = 325 nm for **P6**; 370 nm for hb-**P1**; 360 nm for hb-**P2**; 300 nm for hb-**P3**. (C and F) Plot of the relative PL intensity (I/I_0) *versus* the composition of the aqueous mixture of **P6** and hb-**P1**–hb-**P3**. I_0 = intensity at f_w = 0%. Inset: fluorescence photographs of the THF solutions of polymers **P6** and hb-**P1**–hb-**P3** and their aggregates in THF/water mixtures with different f_ws. All fluorescence photographs were taken under UV irradiation at 365 nm.

known fluorophore that is widely used for the design of functional fluorescent materials.[42] The incorporation of TPE and/or a TPA moiety in PODs could endow these polymers with interesting PL behaviors. We thus systematically investigated the PL properties of the TPE- and/or TPA-containing PODs in THF solutions and THF/water mixtures with different water fractions (f_w). As depicted in Fig. 5A–C, due to the presence of the TPE moiety in their polymer skeletons, **P6** and hb-**P3** showed typical AIE features. With the gradual addition of water into their THF solutions, the PL intensity of **P6** and hb-**P3** was steadily enhanced and reached the maximum at a f_w of 80% and 70%, respectively. The maximum PL intensity of **P6** aggregates was 9.4-fold higher than that of its pure THF solution, while a 3.8-fold increase in PL intensity was observed for hb-**P3** after aggregation. The fluorescence quantum yields (Φ_f) of **P6** and hb-**P3** in different states further confirmed their AIE characteristics (Table S2†). The weakly emissive THF solution of **P6** with a Φ_f of 0.6% increased to 4.5% when f_w reached 80%, whereas Φ_f of green-emissive hb-**P3** increased from 3.9% (pure THF solution) to 14.1% (f_w = 70%). The remarkably higher PL efficiencies of the hyperbranched polymer hb-**P3** in THF solution and aggregated states than those of the linear polymer **P6** might be ascribed to the inherently stronger restriction of the intramolecular motions of TPE units in the hyperbranched polymer chains as well as the presence of much richer intra-/inter-chain interactions upon aggregation.[43,44]

In contrast, the TPA-containing polymer hb-**P1** showed an aggregation-caused quenching effect with strong blue fluorescence in the solution state (Fig. 5D and F). A similar phenomenon was also observed for hb-**P2** (Fig. 5E and F), which indicates that the introduction of TPE is not effective to endow hb-**P1** with AIE properties. The UV-vis absorption spectra of hb-**P1** and hb-**P2** in different states were then compared with the PL spectrum of TPE. As depicted in Fig. S11,† the PL spectrum of TPE overlapped with the absorption spectrum of hb-**P2** aggregates to a larger degree than those of hb-**P2** solution and hb-**P1**. We thus speculated that the unexpected weak fluorescence of hb-**P2** in the aggregated state might result from the energy transfer from the excited state of the TPE luminogen to the ground state of the TPA-containing conjugated moiety.[45] Because the TPE moiety of hb-**P2** is linked with the TPA-phenyloxadiazole moiety in a non-conjugated manner and meanwhile TPE is non-emissive in the solution state, it is reasonable that the PL properties of hb-**P2** solution are similar to those of hb-**P1** solution.

Formation and visualization of microporous film morphologies

Attracted by the excellent film-forming capability and potential self-assembly properties of PODs as reported in the literature,[46] we then investigated the film-forming and assembly behaviors of the obtained polymers with **P3** as an example. As depicted in Fig. S12,† the dilute chloroform solution of **P3** at a concentration of 0.01 mg mL^{-1} could form very thin films after evaporation at room temperature. Interestingly, when the solution concentration

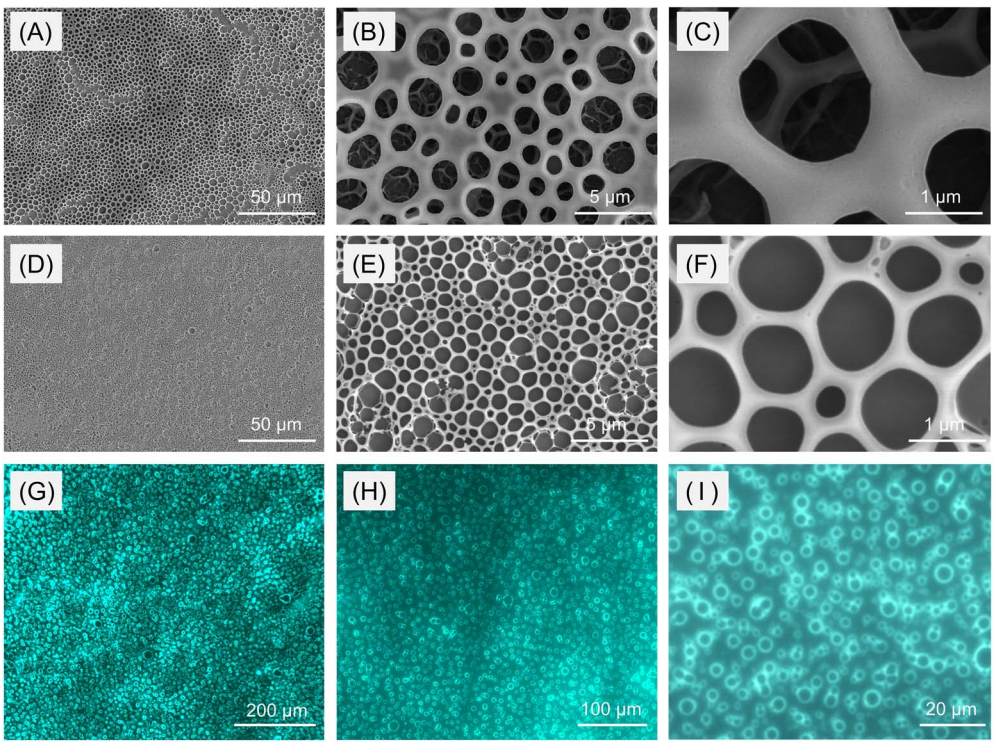

Fig. 6 (A–C) SEM images of the porous thin films prepared by the solvent evaporation of the chloroform solution of **P3** (0.1 mg mL^{-1}) on silicon wafers. (D–F) SEM images and (G–I) fluorescence images of the porous thin films formed by the solvent evaporation of the chloroform solution of **P6** (1.0 mg mL^{-1}) on silicon wafers. Excitation wavelength = 400–440 nm. All these films were prepared on rainy days with an air humidity of above 80%.

was increased to 0.1 mg mL^{-1}, an ordered microporous structure was observed in the thin film under a scanning electron microscope (SEM, Fig. 6A–C). Inspired by this serendipity, we further characterized the film morphology of the AIE-active linear polymer (**P6**) to achieve fluorescent microporous films. Different from **P3**, the evaporation of the chloroform solution of **P6** with a concentration of 0.1 mg mL^{-1} generated a fluorescent thin film with a non-porous structure (Fig. S13†). However, as evidenced by the SEM and fluorescence images in Fig. 6D–I, increasing the solution concentration of **P6** to 1.0 mg mL^{-1} can produce fluorescent microporous films, and these porous structures can be readily observed by fluorescence microscopy. Considering that these microporous films can only be obtained on rainy days, we speculated that the formation of such a pattern might also result from a BF process at high humidity (≥80%) in air.

Polymers that can form stable and ordered microporous films have attracted wide interest in the past few decades due to their potential applications in various fields, such as separation, optoelectronic devices, electrochemical energy systems, cell or bacteria culture, tissue engineering, *etc.*[47–52] The combination of a porous structure and PL performance could further impart materials with potential fluorescence-sensing capabilities. As a commonly used method for the preparation of ordered microporous or honeycomb-structured films, the BF patterning method with water droplets as the sacrificial templates has been demonstrated to be effective for diverse polymeric materials, including amphiphilic copolymers, star polymers, hyperbranched polymers, polymeric polyion materials, and organic–inorganic hybrids.[53–55] Compared with other templating and lithography methods, the BF approach shows the advantages of simplicity, low cost, spontaneous occurrence, and large area applicability. However, the BF method has rarely been applied for the fabrication of luminescent porous films using homogeneous polymer systems.[56] Motivated by the microporous self-assembly morphology of **P6** obtained at high humidity, we next tried to employ the standard static BF process to obtain fluorescent thin films with stable and ordered microporous arrays.

Fig. 7A and S14† show the experimental set-up for the preparation of ordered porous thin films of **P6** by the static BF process. First, a silicon wafer was placed and sealed in a vessel saturated with water vapor. Then the solution of **P6** was cast onto the silicon wafer through the plastic wrap using a syringe, and the pinhole on the plastic wrap was immediately sealed with transparent tape. Finally, the sealed vessel was placed at room temperature for 30 min to allow the spontaneous interfacial self-assembly of **P6** solution in a humid environment. As depicted in Fig. 7B–D, depending on the way in which the humid environment was established, fluorescent honeycomb-patterned films with an adjustable pore size and uniformity could be obtained. In an initial attempt, the experimental device was sealed at room temperature for 2 h to make the water vapor saturated before casting the chloroform solution (1.0 mg mL^{-1}) of **P6** on the substrate (method I). This method can produce an efficiently fluorescent thin film with a microporous structure, but the shape and size uniformity of these pores needed to be further improved (Fig. 7B). Then we tried to first seal the whole device at room temperature for 30 min and then heat the bottom of the vessel at around 70 °C for 2 min to accelerate the saturation of water vapor (method II). Under this condition, a fluorescent microporous film with more ordered morphology and a uniform pore size (diameter = 10.2 ± 1.5 μm; sample size = 200) was produced (Fig. 7C). On the other hand, when the experimental device was only heated at around 70 °C for 2 min before adding the polymer solution (method III), the obtained porous film possessed obviously poorer porosity and a lower film-pore fluorescence contrast (Fig. 7D). Therefore, method II was chosen to be the optimal approach to create a humid environment for the BF patterning of **P6** films.

As illustrated in Fig. 7A, the formation of porous **P6** films through the BF process was supposed to include several steps: (1) evaporation of organic solvent to reduce the air/solution interface temperature below the dew point; (2) condensation of water vapor on the cold solution surface to form water droplets together with the self-organization of water droplets into an ordered droplet array as a patterning template; (3) complete evaporation of the solvent and water droplets to produce the porous polymer film on the substrate. The brighter peripheries around the non-emissive pores suggested that the polymer solute tends to accumulate or precipitate in the interface between polymer solution and water droplets during the solvent evaporation. Taking advantage of the efficient solid-state fluorescence of **P6**, the effects of other preparation conditions on the formation of BF morphology for this novel POD system were further investigated by directly visualizing the morphology using a fluorescence microscope. The results shown in Fig. 7B–G suggested that uniform microporous structures could only be obtained from the chloroform solution of **P6**. Other commonly used solvents in the BF method, including toluene, THF, and DCM, all showed negative effects for **P6** to form porous films possibly due to the relatively poor solubility of **P6** in toluene, the good water miscibility of THF, and the inappropriate solvent volatility of DCM for this polymer system. The screening results on the concentration of the chloroform solution of **P6** suggested that the best BF morphology was obtained at 1.0 mg mL^{-1} (Fig. 7B). Decreasing the solution concentration to 0.5 mg mL^{-1} led to an irregular and disordered porous structure (Fig. 7H), while increasing the concentration to 2.0 and 5.0 mg mL^{-1} significantly reduced the porosity and the pore size (Fig. 7I and J). Such results are consistent with the proposed mechanism for the formation of porous polymer films. The polymer concentration could affect the viscosity and density of the casting solution, thereby influencing the condensation process of water droplets on the solution surface.[53,54]

The BF structures of **P6** films were also characterized by SEM (Fig. S15†), which further confirmed the conclusion drawn from the fluorescence images. Compared with traditional characterization methods such as SEM and TEM for the study of BF formation, the fluorescence imaging technique is much simpler, more sensitive and informative, and less expensive. The obtained BF morphology can be directly observed under a fluorescence microscope without tedious sample treatment procedures. In addition to linear polymers, we also tried to fabricate BF patterns using the hyperbranched AIE polymer (hb-**P3**). However, hb-**P3** cannot generate regular porous films under the above-mentioned fabrication conditions, indicating that the

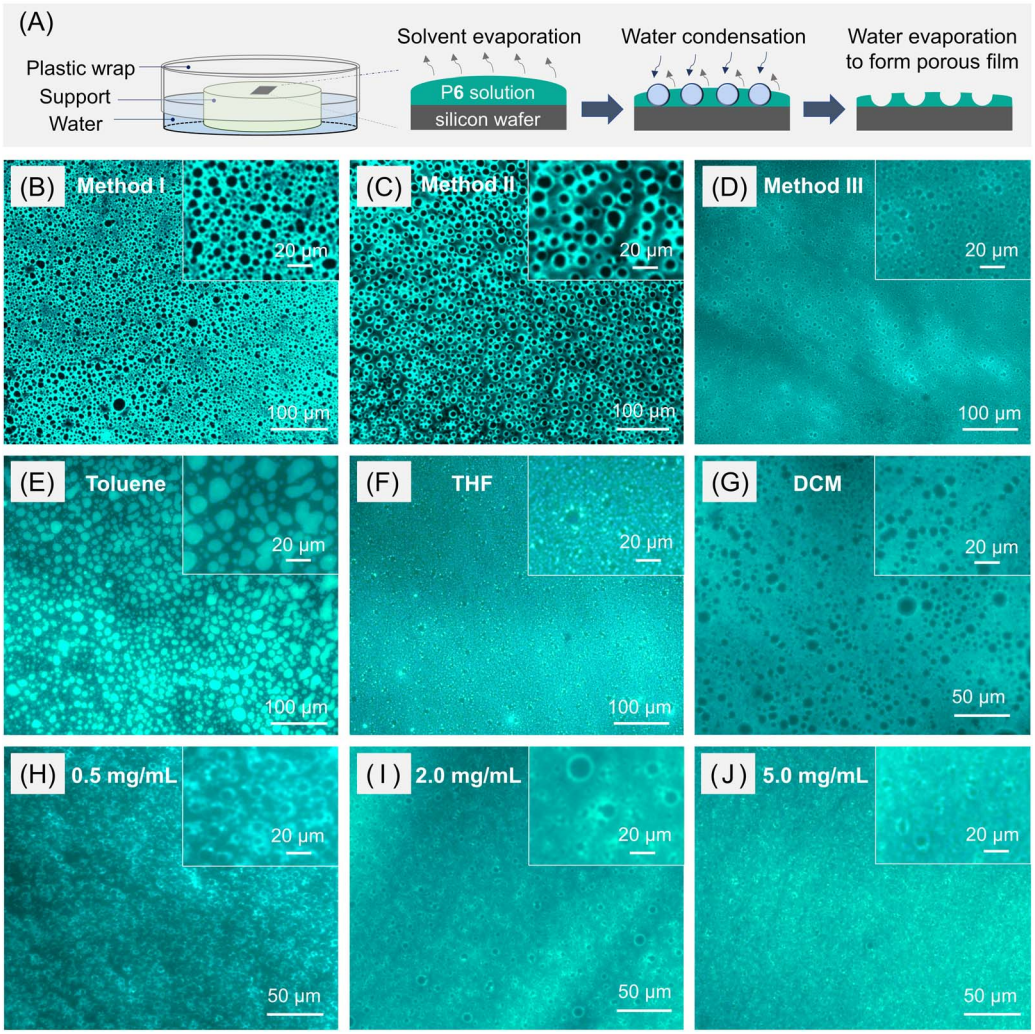

Fig. 7 (A) Schematic illustration of the experimental set-up and the formation mechanism for the preparation of porous films of P6 by the static breath figure process. (B–D) Fluorescence images of the film morphology formed by the chloroform solution of P6 (1.0 mg mL^{-1}) using different methods of establishing a humid environment. (E–G) Fluorescence images showing the influence of organic solvents on the film morphology of P6. Solution concentration: 1.0 mg mL^{-1}. (H–J) Fluorescence images showing the influence of the concentration of the chloroform solution of P6 on the film morphology. Excitation wavelength = 400–440 nm.

topological polymer structures might greatly influence the formation capability of microporous BF structures.

Cell imaging

Considering the catalyst-free characteristic of this MCP and the advantages of AIE polymers as fluorescence imaging reagents,[57] we then explored the application of the obtained AIE-active PODs in cell imaging. The cell staining capability of **P6** was first evaluated using a confocal laser scanning microscope (CLSM). As shown in Fig. S16,† bright blue fluorescence was observed in 4T1 cells after incubation with **P6**, indicating its good cell staining ability. Closer inspection suggested that **P6** might specifically stain the lysosomes of 4T1 cells, which was further verified by the co-staining result of **P6** with a commercial lysosome imaging probe (LysoTracker Red, LTR; Fig. S17†). However, the cytotoxicity of **P6** needed to be further improved as suggested by the 3-(4,5-dimethyl-2-thiazolyl)-2,5-diphenyltetrazolium bromide (MTT) cell-viability assay result (Fig. S18†). To solve this issue, **P6** was prepared into NPs through a nanoprecipitation method with a biocompatible amphiphilic copolymer DSPE-PEG2000 as the encapsulation matrix. The obtained **P6** NPs indeed showed much better biocompatibility toward 4T1 cells (Fig. 8A). Similarly, the biocompatibility of the AIE-active hyperbranched polymer hb-**P3** NPs was also found to be much better than that of its DMSO stock solution (Fig. S19† and 8A). No significant change was observed in the cell viability after incubation with **P6** NPs or hb-**P3** NPs at a high concentration of up to 50 μg mL^{-1}. The cell viability can remain about 94% and 85%, respectively, for **P6** NPs and hb-**P3** NPs at a concentration of 100 μg mL^{-1}. The cell imaging experiments were subsequently conducted by costaining 4T1 cells with LTR and polymer NPs. As depicted in Fig. 8C–J, the staining regions of **P6** NPs and hb-**P3** NPs overlapped with those of LTR to a large extent. The Pearson correlation coefficient of **P6** NPs and hb-**P3** NPs for 4T1 cells was calculated to be 0.79 and 0.83,

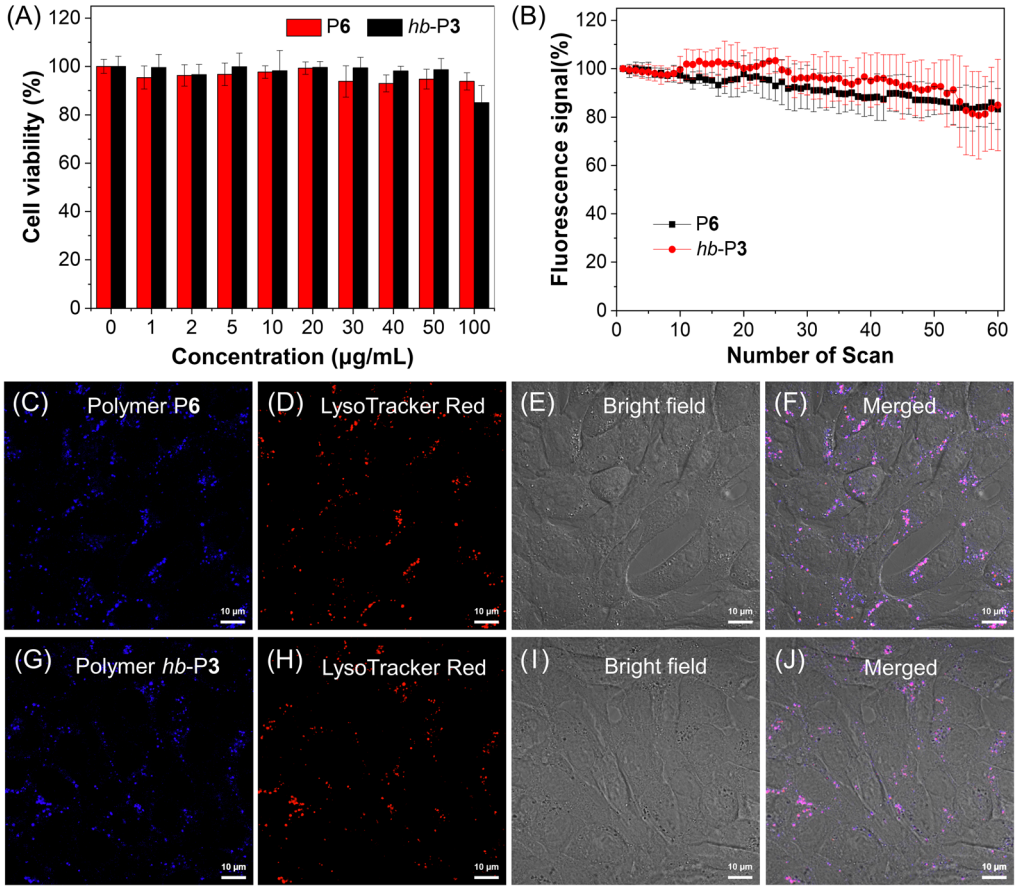

Fig. 8 (A) Cell viability of 4T1 cells in the presence of **P6** and hb-**P3** nanoparticles (NPs) at different concentrations. (B) Change in the fluorescence signal from 4T1 cells stained with **P6** and hb-**P3** NPs (20 μg mL^{-1}, 4 h) with the number of scans. (C–F) Confocal images of 4T1 cells stained with (C) **P6** NPs (20 μg mL^{-1}, 4 h) and (D) LysoTracker Red (LTR, 1 μM, 30 min) and (E) the bright-field image as well as (F) their merged image. (G–J) Confocal images of 4T1 cells stained with (G) hb-**P3** NPs (20 μg mL^{-1}, 4 h) and (H) LysoTracker Red (LTR, 1 μM, 30 min) and (I) the bright-field image as well as (J) their merged image. Scale bar = 10 μm. Excitation wavelength: 405 nm for polymers and 561 nm for LTR; emission filter: 420–650 nm for polymers and 650–700 nm for LTR.

respectively. These results indicated that these polymer NPs showed good specificity for lysosomes. Furthermore, both **P6** NPs and hb-**P3** NPs showed excellent photostability. There was no remarkable signal loss after continuous irradiation at 405 nm excitation for 60 scans (Fig. 8B and S20†). The excellent biocompatibility, good lysosome specificity, and excellent photobleaching resistance enable the obtained AIE-active PODs to function as promising lysosome-specific fluorescent probes in biological imaging.

Conclusions

In summary, we have developed a novel Ugi-type MCP tool for the facile synthesis of functional PODs with diverse topological structures and attractive properties. Unlike conventional Ugi polycondensations, the present MCPs can *in situ* generate oxadiazole moieties in polymer backbones because of the remarkably different reaction mechanism arising from the use of (*N*-isocyanimino)triphenylphosphorane and secondary amines as the monomers. Compared with traditional synthetic methods toward PODs, this catalyst-free MCP strategy enjoys the advantages of readily available monomers, simple operation, mild reaction conditions, and well-defined structures. The structures of the resulting PODs can be flexibly adjusted by adopting different monomer combinations, including $A_2 + B_2 + C_1 + D_1$, $A_2 + B_3 + C_1 + D_1$, and $A_2 + B_4 + C_1 + D_1$. Through these MCPs, a series of linear and hyperbranched PODs with high molecular weights and good solubility in common organic solvents were readily prepared at room temperature. The produced POD structures are hard to achieve by other polymerization methods. All the obtained polymers possess good thermal and morphological stability and excellent film-forming ability. The inherent structural features of these non-conjugated PODs and the appropriate introduction of AIE moieties into polymer backbones endow the resulting polymers with efficient aggregate-state fluorescence. Taking advantage of the good film-forming ability, self-assembly properties, and bright solid-state fluorescence of the AIE-active linear PODs, fluorescent thin films with stable and ordered microporous structures were prepared based on the simple BF patterning method. The influence factors for PODs to form ordered microporous films were systematically investigated and the BF morphologies can be directly visualized by fluorescence

microscopy in a simple, sensitive, on-site and real-time manner, which could facilitate further study on the applications of such fluorescent porous thin films in different fields. In addition to the direct visualization of self-assembly morphologies, the efficient aggregate-state fluorescence of the obtained AIE polymers also enables them to find applications in biological imaging. The NPs of both the linear AIE-active PODs and the hyperbranched ones can function as promising lysosome-specific fluorescent probes with excellent biocompatibility, good lysosome specificity, and excellent photobleaching resistance. The new and facile synthetic strategy, diverse polymer structures, systematic study of the structure–property relationship, and fascinating functionalities of the obtained polymers in this work will provide informative insights for researchers from different areas to further design, synthesize, and explore the advanced applications of diversified functional heterocyclic polymer materials.

Data availability

All of the experimental data associated with this study are available in the ESI.†

Author contributions

J. X. performed the synthesis, structural characterization, thermal and photophysical measurements, and fabrication of the microporous films. N. N performed the cell imaging studies. X. F. performed the measurement of absolute molecular weights. X. S., D. W., and A. Q. participated in the experimental design, data analysis and discussion. T. H. and B. Z. T. conceived and designed the experiments and supervised the overall project. J. X., T. H., and B. Z. T. wrote and revised the paper with the contribution of all other authors.

Conflicts of interest

There are no conflicts to declare.

Acknowledgements

This work was supported by the National Natural Science Foundation of China (grant no. 21905176 and 22271197), the Natural Science Foundation for Distinguished Young Scholars of Guangdong Province (grant no. 2020B1515020011), and the Science and Technology Plan of Shenzhen (grant no. JCYJ20190808142403590, JCYJ20220531102601003, and JCYJ20190808153415062). The authors also acknowledge the Instrumental Analysis Center of Shenzhen University.

Notes and references

1 J. Li, J. Wang, Z. Wu, S. Tao and D. Jiang, *Angew. Chem., Int. Ed.*, 2021, **60**, 12918–12923.
2 F. Vidal and F. Jäkle, *Angew. Chem., Int. Ed.*, 2019, **58**, 5846–5870.
3 M. Zhang, S. Dai, S. Chandrabose, K. Chen, K. Liu, M. Qin, X. Lu, J. M. Hodgkiss, H. Zhou and X. Zhan, *J. Am. Chem. Soc.*, 2018, **140**, 14938–14944.
4 T. Wang, N. Zhang, W. Bai and Y. Bao, *Polym. Chem.*, 2020, **11**, 3095–3114.
5 L. Lu, W. Chen, T. Xu and L. Yu, *Nat. Commun.*, 2015, **6**, 7327.
6 H. Maab and S. Pereira Nunes, *J. Membr. Sci.*, 2013, **445**, 127–134.
7 J. Xu, N. M. Srivatsa Bettahalli, S. Chisca, M. K. Khalid, N. Ghaffour, R. Vilagines and S. P. Nunes, *Desalination*, 2018, **432**, 32–39.
8 Z. Yuan, X. Li, Y. Duan, Y. Zhao and H. Zhang, *J. Membr. Sci.*, 2015, **488**, 194–202.
9 Y. Yu, H. Gao, J. Zhu, D. Li, F. Wang, C. Jiang, T. Zhong, S. Liang and M. Jiang, *Chin. Chem. Lett.*, 2021, **32**, 203–209.
10 G.-S. Liou, S.-H. Hsiao, W.-C. Chen and H.-J. Yen, *Macromolecules*, 2006, **39**, 6036–6045.
11 M. Li, V. Karanikola, X. Zhang, L. Wang and M. Elimelech, *Environ. Sci. Technol. Lett.*, 2018, **5**, 266–271.
12 B. S. Gaylord, S. Wang, A. J. Heeger and G. C. Bazan, *J. Am. Chem. Soc.*, 2001, **123**, 6417–6418.
13 D. Gomes, S. P. Nunes, J. Carlos Pinto and C. Borges, *Polymer*, 2003, **44**, 3633–3639.
14 D. Gomes, J. Roeder, M. L. Ponce and S. P. Nunes, *J. Power Sources*, 2008, **175**, 49–59.
15 H. Xue, Y. Zhao, H. Wu, Z. Wang, B. Yang, Y. Wei, Z. Wang and L. Tao, *J. Am. Chem. Soc.*, 2016, **138**, 8690–8693.
16 Z. Zhang, Y.-Z. You, D.-C. Wu and C.-Y. Hong, *Macromolecules*, 2015, **48**, 3414–3421.
17 L. V. Kayser, M. Vollmer, M. Welnhofer, H. Krikcziokat, K. Meerholz and B. A. Arndtsen, *J. Am. Chem. Soc.*, 2016, **138**, 10516–10521.
18 X. Wu, H. Lin, F. Dai, R. Hu and B. Z. Tang, *CCS Chem.*, 2020, **2**, 191–202.
19 Y. Hu, N. Yan, X. Liu, L. Pei, C. Ye, W.-X. Wang, J. W. Y. Lam and B. Z. Tang, *CCS Chem.*, 2022, **4**, 2308–2320.
20 T. Han, H. Deng, Z. Qiu, Z. Zhao, H. Zhang, H. Zou, N. L. C. Leung, G. Shan, M. R. J. Elsegood, J. W. Y. Lam and B. Z. Tang, *J. Am. Chem. Soc.*, 2018, **140**, 5588–5598.
21 H. Kim, K. T. Bang, I. Choi, J. K. Lee and T. L. Choi, *J. Am. Chem. Soc.*, 2016, **138**, 8612–8622.
22 J. Peng, N. Zheng, P. Shen, Z. Zhao, R. Hu and B. Z. Tang, *Chem*, 2022, **8**, 2301–2316.
23 P. Liu, W. Fu, P. Verwilst, M. Won, J. Shin, Z. Cai, B. Tong, J. Shi, Y. Dong and J. S. Kim, *Angew. Chem., Int. Ed.*, 2020, **59**, 8435–8439.
24 A. Sehlinger, P.-K. Dannecker, O. Kreye and M. A. R. Meier, *Macromolecules*, 2014, **47**, 2774–2783.
25 P. Stiernet and A. Debuigne, *Polym. Sci.*, 2022, **128**, 101528.
26 B. Yang, Y. Zhao, Y. Wei, C. Fu and L. Tao, *Polym. Chem.*, 2015, **6**, 8233–8239.
27 N. Gangloff, D. Nahm, L. Döring, D. Kuckling and R. J. Luxenhofer, *J. Polym. Sci., A: Polym. Chem.*, 2015, **53**, 1680–1686.
28 X. Zhang, S. Wang, J. Liu, Z. Xie, S. Luan, C. Xiao, Y. Tao and X. Wang, *ACS Macro Lett.*, 2016, **5**, 1049–1054.

29 Y. Tao, J. Chen, S. Wang and Y. Tao, *Acta Polym. Sin.*, 2020, **51**, 738–743.
30 A. Al Samad, J. De Winter, P. Gerbaux, C. Jérôme and A. Debuigne, *Chem. Commun.*, 2017, **53**, 12240–12243.
31 M. Hartweg and C. R. Becer, *Green Chem.*, 2016, **18**, 3272–3277.
32 A. Sehlinger, R. Schneider and M. A. Meier, *Macromol. Rapid Commun.*, 2014, **35**, 1866–1871.
33 J. Zheng, C. Fu, Z. Chen, P. Zhang, R. Zhao, L. Ding, H. Liu and K. Deng, *Polym. Adv. Technol.*, 2022, **33**, 1978–1988.
34 A. Ramazani and A. Rezaei, *Org. Lett.*, 2010, **12**, 2852–2855.
35 H. G. O. Alvim, E. N. da Silva Júnior and B. A. D. Neto, *RSC Adv.*, 2014, **4**, 54282–54299.
36 P. J. Flory, *Principles of Polymer Chemistry*, Cornell University Press, Ithaca, NY, 1953.
37 S. Unal and T. E. Long, *Macromolecules*, 2006, **39**, 2788–2793.
38 B. Yao, T. Hu, H. Zhang, J. Li, J. Z. Sun, A. Qin and B. Z. Tang, *Macromolecules*, 2015, **48**, 7782–7791.
39 T. Han, D. Yan, Q. Wu, N. Song, H. Zhang and D. Wang, *Chin. J. Chem.*, 2021, **39**, 677–689.
40 J. Yang, M. Fang and Z. Li, *Aggregate*, 2020, **1**, 6–18.
41 Z. Zhao, J. W. Y. Lam and B. Z. Tang, *J. Mater. Chem. A*, 2012, **22**, 23726–23740.
42 H.-J. Yen and G.-S. Liou, *Prog. Polym. Sci.*, 2019, **89**, 250–287.
43 J. Guan, C. Shen, J. Peng and J. Zheng, *J. Phys. Chem. Lett.*, 2021, **12**, 4218–4226.
44 Q. Li and Z. Li, *Acc. Chem. Res.*, 2020, **53**, 962–973.
45 H. Deng, Z. He, J. W. Y. Lam and B. Z. Tang, *Polym. Chem.*, 2015, **6**, 8297–8305.
46 J. Zhu, Z. Dong, S. Lei, L. Cao, B. Yang, W. Li, Y. Zhang, J. Liu and J. Shen, *Angew. Chem., Int. Ed.*, 2015, **54**, 3097–3101.
47 J. Liang, Z. Song, S. Wang, X. Zhao, Y. Tong, H. Ren, S. Guo and Q. T. Y. Liu, *ACS Appl. Mater. Interfaces*, 2020, **12**, 52992–53002.
48 J. Li and Z. He, *Environ. Sci. Water Res. Technol.*, 2015, **1**, 355–362.
49 Y. Tao, H. Liu, H.-Y. Kong, T.-X. Wang, H. Sun, Y. J. Li, X. Ding, L. Sun and B.-H. Han, *Angew. Chem., Int. Ed.*, 2022, **61**, e202205796.
50 J. R. Varcoe, P. Atanassov, D. R. Dekel, A. M. Herring, M. A. Hickner, P. A. Kohl, A. R. Kucernak, W. E. Mustain, K. Nijmeijer, K. Scott, T. Xu and L. Zhuang, *Energy Environ. Sci.*, 2014, **7**, 3135–3191.
51 L. Chen, C. Yan and Z. Zheng, *Mater. Today*, 2018, **21**, 38–59.
52 T. Kuang, S. Chen, Z. Gu, Z. Shen, A. Hejna, M. Saeb, F. Chen, M. Zhong and T. Liu, *Hybrid Mater.*, 2022, **5**, 1376–1384.
53 Y. Dou, M. Jin, G. Zhou and L. Shui, *Membranes*, 2015, **5**, 399–424.
54 H. Bai, C. Du, A. Zhang and L. Li, *Angew. Chem., Int. Ed.*, 2013, **52**, 12240–12255.
55 R. Hu, J. W. Y. Lam, M. Li, H. Deng, J. Li and B. Z. Tang, *J. Polym. Sci., A: Polym. Chem.*, 2013, **51**, 4752–4764.
56 J. Li, Y. Li, C. Y. K. Chan, R. T. K. Kwok, H. Li, P. Zrazhevskiy, X. Gao, J. Z. Sun, A. Qin and B. Z. Tang, *Angew. Chem., Int. Ed.*, 2014, **53**, 13518–13522.
57 P. Xiao, K. Ma, M. Kang, L. Huang, Q. Wu, N. Song, J. Ge, D. Li, J. Dong, L. Wang, D. Wang and B. Z. Tang, *Chem. Sci.*, 2021, **12**, 13949–13957.